PCCP

Accepted Manuscript

ROYAL SOCIETY OF CHEMISTRY

www.rsc.org/pccp

Physical Chemistry Chemical Physics
CREATED USING THE RSC LaTeX PCCP ARTICLE TEMPLATE – SEE www.rsc.org/electronicfiles FOR DETAILS
ARTICLE TYPE www. rsc.org/xxxxxx | XXXXXXXX

Electron transfer within a reaction path model calibrated by constrained DFT calculations: Application to mixed-valence organic compounds

E. Mangaud [a,b], A. de la Lande[b], C. Meier[a] and M. Desouter-Lecomte[b,c]

Received Xth XXXXXXXXXX 20XX, Accepted Xth XXXXXXXXX 20XX
First published on the web Xth XXXXXXXXXX 200X
DOI: 10.1039/b000000x

The quantum dynamics of electron transfer in mixed-valence organic compounds is investigated using a reaction path model calibrated by constrained density functional theory (cDFT). Constrained DFT is used to define diabatic states relevant for describing the electron transfer, to obtain equilibrium structures for each of these states and to estimate the electronic coupling between them. The harmonic analysis at the diabatic minima yields normal modes forming the dissipative bath coupled to the electronic states. In order to decrease the system-bath coupling, an effective one dimensional vibronic Hamiltonian is constructed by partitioning the modes into a linear reaction path which connects both equilibrium positions and a set of secondary vibrational modes, coupled to this reaction coordinate. Using this vibronic model Hamiltonian, dissipative quantum dynamics is carried out using Redfield theory, based on a spectral density which is determined from the cDFT results. In a first benchmark case, the model is applied to a series of mixed-valence organic compounds formed by two 1,4-dimethoxy-3-methylphenylen fragments linked by an increasing number of phenylen bridge. This allows us to examine the coherent electron transfer in extreme situations leading to a ground adiabatic state with or without barrier and therefore to a trapping of the charge or to an easy delocalization.

1 Introduction

Electron transfer (ET) in organic or inorganic chemical and in biological systems has received a widespread interest [1–3] and remains a challenging subject both experimentally and theoretically. Electron transfer is central in many redox biological processes [4,5] but also in the dissociation of excitons at heterojunctions in photovoltaic materials [6–10] or in molecular electronics [11]. It is intrinsically a nonadiabatic process involving at least two electronic states, and the recent observation that quantum coherence can survive for a surprisingly long time even in biological systems [12–16] at room temperature has renewed the interest in modelling such quantum processes in complex environments. Long-lived coherences imply that the quantum system remains in a superposition of states before reaching the Boltzmann equilibrium. To explore this relaxation process, the basic tool is a system-bath Hamiltonian [17,18] in which the system consists of the two electronic states and the bath models the environment, usually by harmonic oscillators or phonon modes. The usual Donor-Acceptor view corresponds to the diabatic electronic representation and the main parameter is the electronic coupling responsible for the transfer. In this context, however, obtaining the relevant diabatic states remains a challenge in large molecules, and is still currently investigated using different strategies [6,19–31].

In this work, we address the ab-initio calibration of the diabatic system-bath Hamiltonian by cDFT [32–34](constrained density functional theory) which is particularly appealing since it constrains the electron density optimization to define ad hoc the diabatic electronic states. Here, each state results from a particular optimization of the ground state with a constrained distribution of the electronic density. Subsequently, ET dynamics is analyzed by a method for open quantum systems. The crudest approach is the spin-boson model in which the system is restricted to the two electronic states at their equilibrium geometries and the bath is formed by all vibrational modes. This two-level dissipative model might lead to a strong coupling of the electronic degrees of freedom with the vibrations, possibly not allowing for a perturbative treatment. In this case, one might resort to non-perturbative methods, like those based on path integrals [35,36], or on the Hierarchic Equations of Motions (HEOM) method [13,37–40], or to a full-dimensional dynamical treatment using the Multi-Configuration Time dependent Hartee (MCTDH) methodology [41–44], possibly in its recent multi-layer formulation (ML-MCTDH) [45–48].

[a] *Laboratoire Collisions Agrégats Réactivité, UMR 5589, IRSAMC, Université Toulouse III Paul Sabatier, Bât. 3R1b4, 118 route de Narbonne, F-31062, Toulouse, France.*
[b] *Laboratoire de Chimie Physique, UMR 8000, Université Paris-Sud, Bât. 349, 15 avenue Jean Perrin, F-91405 Orsay, France.*
[c] *Département de Chimie, Université de Liège, Sart Tilman, B6, B-4000 Liège, Belgium.*

An alternative route is to augment the system dimensionality by including certain vibrational degrees of freedom into the system such that the coupling to the remaining bath is reduced[17,49–52]. In this work, we follow this latter strategy. Specifically, the primary normal modes are partitioned into a linear reaction path coordinate which connects the two equilibrium diabatic structures (to be considered as part of the system) and secondary modes which form the new bath. These new bath modes are chosen to be orthogonal, but coupled to the reaction path. This approach is one of the possible reaction coordinate representation of the spin-boson model providing the usual Marcus scheme[53] with two crossing diabatic potential energy curves. This strategy has been frequently discussed in dissipative dynamics[54–58]. Note that the definition of the reaction coordinate is not unique, and alternative choices exist, which will be discussed.

Once a system / bath separation is obtained which allows for a perturbative treatment, a wide range of dynamical methods exist, like semiclassical[59–61], quantum[35,36] or stochastic methods[62,63]. Their validity with respect to the dynamical regime are reviewed for example in Ref.[64].

In this work, we model the dissipative dynamics based on the Bloch-Redfield approach[65–67], which has proven its usefulness in various applications[68–71]. It is based not only on a weak coupling assumption, but also on the Markov approximation, valid when the bath correlation functions decays rapidly as compared to the typical system timescales. Note that this constraint can be overcome by non-Markovian methods[72–75], and the vibronic Hamiltonian developed in this work could in the future be directly used within this framework.

Organic mixed-valence compounds[76] can be investigated as model system for electron transfer. The chosen system is composed of 1,4-dimethoxy-3,methylphenylens groups (DMP) bound by a n-paraphenylens chain (DMP$_n$). DMP$_n$ are organic mixed-valence compounds[77,78] in their +I degree of oxidation. The donor and acceptor sites of these aromatic polymers are bound by an increasing chain of n-paraphenylens rings. This allows us to consider different situations with decreasing electronic coupling and therefore different electron transfer regimes.

The paper is organized as follows. The molecular system is presented in Sec. 2. Sec.3 summarizes the cDFT method and gives the structural results. The vibronic diabatic Hamiltonian calibrated by cDFT and the one-dimensional effective Hamiltonian after the extraction of a reaction path are discussed in Secs. 4 and 5, respectively. The tools for describing the dissipative ET process are then defined in Sec. 6. Finally Sec. 7 analyzes the different dynamical behaviours and temperature effects, before concluding by giving perspectives for future directions.

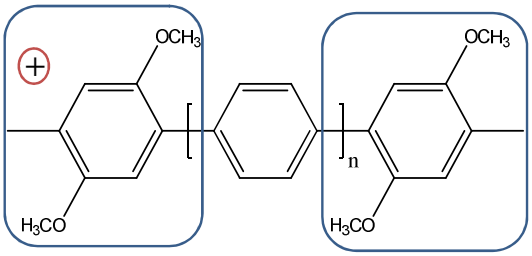

Fig. 1 DMP$_n$: 1,4-dimethoxy-3,methylphenylens groups bound by a chain of n-paraphenylens.

2 Molecular system

We consider 1,4-dimethoxy-3,methylphenylens groups (DMP) bound by a n-paraphenylens chain (DMP$_n$). One of these DMP groups carries a charge. The n value corresponds to the number of paraphenylens cycles (0,1 or 2 in this study) bonding donor and acceptor groups. Our aim is to study the effect of the bridge onto the charge transfer between the acceptor DMP group (positively charged) and the donor (neutral), as shown in Fig. 1. The two diabatic electronic states of the spin-boson model are then degenerate and correspond to the state with the positive charge on the left (L) or the right (R) ring.

Within the Robin-Day classification scheme[79], mixed-valence compounds can be separated in three different classes following the strength of the electronic coupling that represents the ability of the charge to migrate from one site to another. Class I corresponds to the case where the charge is completely localized and cannot move. This corresponds to a vanishing electronic coupling. In class II, a weak electronic coupling leads to a partial delocalization of the charge. In class III, a strong electronic coupling allows the charge to be completely delocalized over the two cycles. Experimental studies[77,78] show that DMP$_0$ is a class III compound (charge of +0.5 on each cycle), whereas DMP$_2$ has all the features of a class II compound (charge +1 localized on one cycle and a weak electronic coupling (around 400 cm^{-1})). Nevertheless, DMP$_1$ exhibits features of class II and class III (charge partially localized +0.8 on acceptor cycle and +0.2 on donor one).

In this work, we study how this classification manifest in the dynamics of the energy transfer and its dynamical interplay with nuclear deformations.

3 Electronic structure

To assess charge transfer dynamics, as well as to analyze geometrical characteristics, extended electronic structure calcu-

lations have been performed, both with constrained DFT and conventional DFT.

3.1 Electronic Structure Calculations

3.1.1 Constrained DFT. cDFT calculations have been performed with a locally modified version[80,81] of the software deMon2k[82]. Resolution of the Kohn Sham equations were performed in the context of auxiliary DFT, meaning that auxiliary electronic density functions are used to compute both the Coulomb and exchange-correlation (XC) contributions to the Kohn-Sham potential[83]. All the calculations was performed with the TZVP (Triple Zeta with Valence Polarization Functions) atomic basis set[84] and the GEN-A2* auxiliary basis set[85]. Adaptive grids of fine mesh have been used to calculate the XC potential[86]. Tolerance criteria of 10^{-9} Ha and 10^{-6} Ha have been used for the SCF (Self Consistent Field) energy and for the density fitting coefficient error. We tested the following XC functionals: OPBE[87,88], OPTX-LYP[89], revPBE98[90], B3LYP[91] and PBE0[88,92]. Calculations with hybrid functionals have been obtained through a variational fitting of the Fock exchange potential[93]. The influence of dispersion interactions on the optimized geometries were found to be negligible (see Supporting Material) and were not included in the results presented below.

Diabatic states relevant to charge transfer processes have been defined with cDFT by imposing the net charge difference[94] between the two extreme aromatic cycles to be equal to one. The atomic charges for cDFT calculations were defined according to the Hirshfeld scheme[95]. Geometry optimizations for each diabatic state have been carried out with tolerance criteria of 10^{-5} Ha/bohr. The normal modes have been calculated under the harmonic approximation from the second derivatives of the energy with respect to the nuclear displacements (Hessian matrix). The Hessian matrix elements have been calculated numerically by the finite differences method. The electronic coupling element between diabatic states are calculated according to the orthogonalization procedure described by Wu and Van Voohris[96].

3.1.2 Standard DFT details. To complement the results obtained by cDFT, we also perform standard DFT calculations using Gaussian09[97]. This enables us to use other XC functionals that were not available in our version of deMon2k such as the long-range corrected (ωB97XD[98]) exchange-correlation functional. The hybrid (M06HF[99]) functional has also been used with Gaussian09. All these calculations have been carried out with a 6-311g** basis, geometry optimization using tight convergence criterion and ultrafine grids. Note that we verified that addition of diffuse functions did not have significant effects on the optimized geometries (see Supplementary Material).

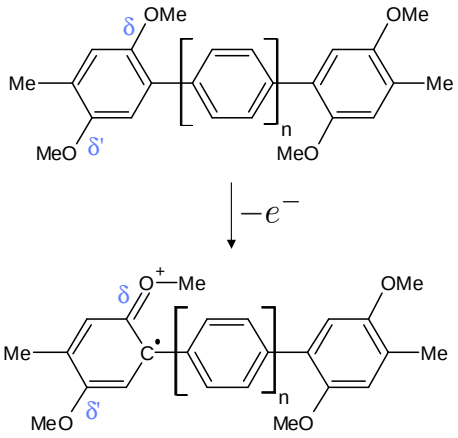

Fig. 2 Lewis structure of DMP_n molecules (upon oxidation, donor cycle have a benzoidal structure whereas the acceptor one exhibits a quinonoidal structure). For clarity, only one mesomeric formula is shown here.

3.2 Results: geometries and electronic coupling

The ET dynamics is determined by the geometical changes and the electronic coupling. In this section, we present results of the geometries as well as the electronic coupling, as obtained by cDFT detailed above.

3.2.1 Geometries. The quality of the geometry is of great importance as it is the main parameter used in the parametrization of the bath. Atomic coordinates of each optimized molecules are reported in supplementary material.

Upon oxidation (see figure 2), a benzoidal-quinonoidal deformation of the acceptor cycle can be noticed on the Lewis representation of the molecule. One can use this general geometric behavior as a parameter to assess how localized the charge is on each cycle[77,78]. In particular, the C-O bond length δ (given in Table 1) becomes shorter as the cycle becomes charged. For DMP_0, the C-O bond length is identical for the D and A cycles, while a difference appears for DMP_1 and which is even more pronounced for DMP_2. This data illustrates the Robin-Day classification of DMP series of molecules. The DFT optimized geometries do not systematically reproduce this trend because of self-interaction-error. With a pure GGA OPBE functional or the hybrid B3LYP functional, the C-O bond length is similar on both sides of the molecules in the three cases. These functionals fail to describe the type II nature of DMP_2. On the opposite, M06HF predicts the three molecules to belong to class II. The range separated functional provides a qualitatively correct picture when comparing the bond lengths with the experimental values. Note however that the use of range separated functionals relies on the empiricism of the determination of the range-separation parameter[100].

To circumvent these difficulties, we use the constrained

Table 1 Variation of C-O bound length δ in of DMP_n (n = 0,1,2) for diabatic (cDFT) or adiabatic states (DFT). A : acceptor cycle / D : donor cycle.

δ bound length	cDFT OPBE		DFT OPBE		DFT B3LYP	
	D	A	D	A	D	A
DMP_0	1.32	1.37	1.34	1.34	1.34	1.34
DMP_1	1.32	1.37	1.35	1.35	1.34	1.34
DMP_2	1.32	1.37	1.35	1.35	1.35	1.35
δ bound length	DFT M06HF		DFT ωB97XD		Exp.	
	D	A	D	A	D	A
DMP_0	1.30	1.36	1.33	1.33	1.341	1.344
DMP_1	1.30	1.36	1.33	1.34	1.331	1.363
DMP_2	1.32	1.36	1.31	1.36	1.325	1.370

DFT approach and define relevant geometries in the diabatic basis. As can be seen from table 1, cDFT provides geometries that correspond well to the D/A^+ description (and also for the D^+/A state, data not shown).

3.2.2 Electronic couplings. In this paragraph, we discuss the influence of the XC functional of the electronic coupling using the OPBE optimized geometry (Table 2). The "Exp." column corresponds to measured ET rates using a Marcus model[77,78]. As expected, the values reflect a decay of the electronic coupling with the D-A distance, even though the decay is very slow, a consequence or the aromatic character of the bridge molecules. The cDFT values are strongly dependent on the amount of Fock exchange included in the Kohn-Sham potential. OPBE (GGA) is clearly unable to produce reliable values since the computed value is larger for DMP_2 than for DMP_1. A monotonic decay is obtained with hybrid functionals, which is more or less pronounced depending of the percentage of non-local exchange. None of the hybrid functional is fully satisfactory, when compared to the experimental values. For DMP_2, the lowest values are obtained with PBE0-50 (366 cm^{-1}), but the value for DMP_0 is too low.

As a consequence, in order to define the electronic coupling for the dynamical calculations to be presented below, we use a linear fit of $\ln(V_{LR,exp}) = -\beta R_{DA} + b$ where R_{DA} is the distance which separates centers of acceptor and donor cycles. For DMP_0 to DMP_2, experimental lengths of R_{DA} are in good agreement with cDFT results. We find $\beta = -0.179$ a.u. and $b = 8.38$ with least square regression and a determination coefficient of 0.977. This approach can be justified in the context of superexchange theory[101,102] , where it can be shown that in tight-binding, second-order perturbation approximations, $V_{LR,exp}$ follows an exponential decay as a function of a single R_{DA} coordinate.

Table 2 Electronic coupling calculated with cDFT OPBE, B3LYP, PBE0, PBE0-50 (PBE0 with 50 % Fock exchange), experimental fitted data and experimental results

$V_{LR}(cm^{-1})$	OPBE	B3LYP	PBE0	PBE0-50	Fit	Exp.
DMP_0	2364	1598	1400	1083	2007	2330
DMP_1	1888	1123	933	608	926	760
DMP_2	2254	940	892	366	427	430

4 Vibronic Hamiltonian

A vibronic coupling Hamiltonian is developed to study the influence of nuclear dynamics onto the ET process, and, vice-versa, to which extent the ET dynamics influences the nuclear dynamics.

4.1 Derivation of the vibronic Hamiltonian

To this end, we start from the geometry obtained by optimization under charge constraints (cDFT) and the normal modes $\tilde{q}_{L,i}$ corresponding to the (L) configuration. Then, the geometry of the (R) configuration is expressed using the normal mode displacements of the (L) configuration. This yields to a two-state quantum Hamiltonian (atomic units are used throughout):

$$H(\tilde{\mathbf{q}}) = \begin{pmatrix} T + V_L(\tilde{\mathbf{q}}) & V_{LR} \\ V_{RL} & T + V_R(\tilde{\mathbf{q}}) \end{pmatrix} \quad (1)$$

with

$$T = -\frac{1}{2}\sum_{i=1}^{M} \frac{\partial^2}{\partial \tilde{q}_i^2} \quad , \quad (2)$$

$$V_L(\tilde{\mathbf{q}}) = \frac{1}{2}\sum_{i=1}^{M} \omega_i^2 \tilde{q}_i^2 \quad , \quad V_R(\tilde{\mathbf{q}}) = \frac{1}{2}\sum_{i=1}^{M} \omega_i^2 \left(\tilde{q}_i + d_i\right)^2 .$$

In this expression, the d_i describe the deformations of the normal modes of the (L) configuration required to match the (R) configuration. In other words, they reflect the shifts of the potential energy minima along each normal mode. The d_i were obtained by first putting the (L) and (R) geometries in Eckart conditions to minimize the contributions from overall rotation and translation. Then, the atomic displacement vector in mass-weighted Cartesian coordinates is projected onto the displacement vectors corresponding to the normal modes of the (L) configuration[103]. As a consequence, the d_i reflect to which extent the different normal modes are affected by the ET process. They are shown as a function of the corresponding normal mode frequencies ω_i in figure 3.

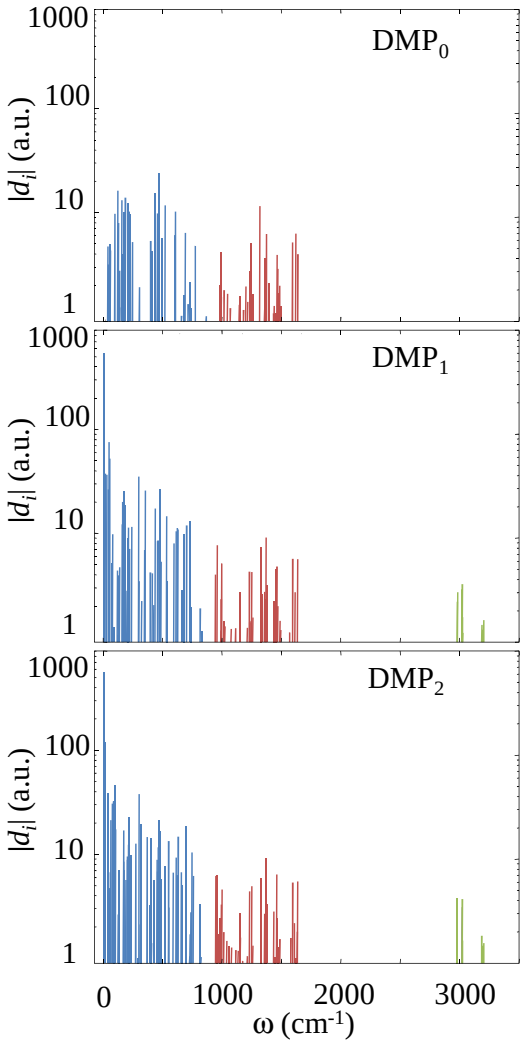

Fig. 3 Absolute value of the normal modes displacements $|d_i|$ in mass-weighted coordinates obtained with the OPBE functional.

4.2 Results for the vibronic Hamiltonian

For all cases, the distribution of $|d_i|$ exhibits three different frequency ranges : below 900 cm^{-1}, we find mainly torsional modes implying the whole molecule, between 900 and 2000 cm^{-1}, there are mainly torsional and stretching modes ($>$ 1300 cm^{-1}) of aromatic carbon skeleton, while frequencies over 2000 cm^{-1} correspond to localized C-H stretching modes.

We want to stress that adding a phenylene ring increases the number of modes by 30, leading to a higher density of states.

Figure 3 shows the $|d_i|$ distribution. Between 900 and 2000 cm^{-1}, it keeps the same form and slightly increases from DMP_0 to DMP_2 even if the number of modes increases by 13 within this frequency range for each phenylene ring. For all DMP_n molecules, cDFT gives geometries for the acceptor and donor ring which are very close, i.e. most of the stretching of the carbon skeleton of the DMP cycles is similarly displaced regardless of the length of the chain. However, the $|d_i|$ corresponding to the frequencies above 2000 cm^{-1} increase tremendously from DMP_0 to DMP_1 and to a lesser extent, from DMP_1 to DMP_2. This can be explained by the role of the bridge even though it does not contribute significantly to the number of modes (increment of only 4 modes per phenylene ring in this frequency range). The modes above 2000 cm^{-1} are directly related to the stretching of carbon-hydrogen bonds. But when considering both donor-acceptor and acceptor-donor geometries of one DMP_n, one can see that because of the non-planarity of the molecule and in particular the plane containing acceptor and donor cycles, hydrogens of methoxy groups terminal cycles cannot be superposed. Thus, even in the normal mode representation, all modes implying these hydrogens (and in particular, stretching modes) are strongly displaced.

5 Coordinate representation of the spin-boson model

The vibronic coupling Hamiltonian presented in equation (1) forms the basis of the dynamical calculations. Due to the large number of modes, a full quantum dynamical treatment is out of reach. A simulation with the promising ML-MCTDH (Multi Layer-Multi Configuration Time Dependent Hartree)[45–48] method could be investigated with this system size. However, for further applications, in which the solvent or protein modes and temperature effects should be taken into account, we present a dynamical analysis based on dissipative quantum dynamics.

5.1 Reaction path model

A dynamical treatment based on dissipative quantum dynamics relies on a partitioning into a 'system' and a 'bath'. A natural separation would be to treat electronic degrees of freedom as system, and all nuclear degrees of freedom as a bath. This leads to the well-known spin-boson model, which has been widely studied both with path integral methods as well as with methods based on reduced master equations[64].

However, we have found this standard approach not to be amenable to a subsequent perturbative treatment, since the coupling of the electronic degrees of freedom to the nuclear motion was found to be too strong. In this case, a general strategy is to include a part of the nuclear dynamics into an extended system, which is subsequently coupled to the remaining nuclear degrees of freedom. To proceed along this direction, we first re-express the normal mode variables by

$q_i = \tilde{q}_i - d_i/2$ to take advantage of the symmetric character of the studied molecules. The Hamitonian thus reads:

$$H(\mathbf{q}) = \begin{pmatrix} T+V_L(\mathbf{q}) & V_{LR} \\ V_{RL} & T+V_R(\mathbf{q}) \end{pmatrix} \quad (3)$$

with

$$T = -\frac{1}{2}\sum_{i=1}^{M}\frac{\partial^2}{\partial q_i^2} \quad (4)$$

$$V_{R/L}(\mathbf{q}) = \frac{1}{2}\sum_{i=1}^{M}\omega_i^2(q_i \pm d_i/2)^2 = \frac{1}{2}(\mathbf{q}\pm\mathbf{c})^T\mathbf{\Lambda}(\mathbf{q}\pm\mathbf{c}) \quad (5)$$

where we have defined the vector $\mathbf{q} = (q_1, \cdots, q_M)$, the vector $\mathbf{c} = (d_1/2, \cdots, d_M/2)$, as well as the diagonal $M \times M$ matrix $\Lambda_{ij} = \delta_{ij}\omega_i^2$ for compactness. Note that V_R corresponds to the minus sign in eq. (5). To single out a specific nuclear motion to be treated dynamically, we re-express the nuclear motion by a new basis $\mathbf{u}_i$ such that

$$\mathbf{q} = \sum_{i=1}^{M} x_i \mathbf{u}_i \quad (6)$$

where one can choose a certain reaction path vector $\mathbf{u}_1$ which shall be included into the system to be described dynamically. In what follows, we choose $\mathbf{u}_1 = \mathbf{c}/\|\mathbf{c}\|$, which means that the reaction path defined by $\mathbf{u}_1$ describes a linear interpolation between the two (L) and (R) structures.

Despite similar in spirit, this ansatz differs from the effective mode methodology put forward in Refs.[51,52,104]. This alternative strategy consists in choosing an effective mode endorsing the whole vibronic coupling, i.e. the vector $\mathbf{g} = \mathbf{\Lambda c}/\|\mathbf{\Lambda c}\|$. The difference between the two selected active coordinates can be illustrated in a two-dimensional case as shown in Fig. 4.

The reference point chosen in this symmetric case coincides either with the minimum of the ground adiabatic state (class III) or with the transition state when this state presents a barrier (class II). The $\mathbf{u_1}$ vector lies along the line connecting the two diabatic minima while the $\mathbf{g}$ vector is the gradient vector of the difference between the two diabatic or adiabatic surfaces. It is orthogonal to the seam or locus where the diabatic surfaces are degenerate. By this way, the only direction inducing a variation of the diabatic or adiabatic energy gap is along this detuning mode. This $\mathbf{g}$ vector is one of the three main vectors used in the description of conical intersections[105]. Vibrations orthogonal to $\mathbf{g}$ are thus decoupled from the electronic system since they do not vary the energy gap but are still coupled to the vibrational motion along $\mathbf{g}$ by cross terms in the potential energy. Fig. 4 depicts contour plots of the diabatic (dashed) and adiabatic surfaces (full lines) for class II and class III systems respectively and the two directions $\mathbf{u_1}$

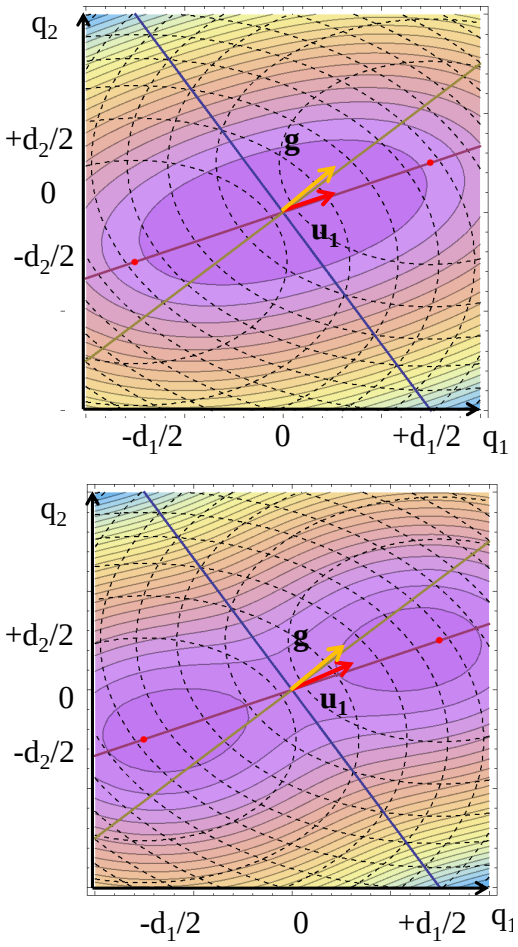

Fig. 4 Two-dimensional representation of the effective mode $\mathbf{g}$ and the reaction path $\mathbf{u}_1$. Upper panel : Class III (without barrier). Lower panel : Class II (with barrier)

and $\mathbf{g}$. One sees that both coordinates present advantages and weak points. Specifically, $\mathbf{u_1}$ really connects the minima and coincides with the minimum energy path near the transition state but does not capture the whole vibronic coupling.

For the present system, we analyzed both possibilities. However, we found that taking $\mathbf{u_1}$ as reaction path, and thus having a reaction path which connects the minima, was important to achieve a weak coupling to the remaining modes, making a subsequent perturbative treatment possible. As a consequence, in what follows, we present results using $\mathbf{u_1}$ as reaction path vector. The remaining $\mathbf{u}_i, i = 2\cdots M$ can be constructed such that

$$\mathbf{u}_i^T\mathbf{u}_j = \delta_{ij} \quad i,j = 1,\cdots,M \quad (7)$$

$$\mathbf{u}_i^T\mathbf{\Lambda}\mathbf{u}_j = \delta_{ij}\tilde{\omega}_i^2 \quad i,j = 2,\cdots,M \quad (8)$$

(see Appendix for details)

Then, both the potentials $V_{L/R}$ and kinetic energies T appearing in eq.(5) can be transformed to yield

$$T = T_1 + T_b \quad (9)$$

$$V_{L/R}(x_1,..x_M) = W_{L/R}(x_1) + \left(x_1 \pm x_1^0\right)\cdot B + V_b(x_2,..,x_M) \quad (10)$$

with

$$T_1 = -\frac{1}{2}\frac{\partial^2}{\partial {x_1}^2} \quad , \quad T_b = -\frac{1}{2}\sum_{i=2}^{M}\frac{\partial^2}{\partial {x_i}^2} \quad (11)$$

$$W_{L/R}(x_1) = \frac{1}{2}\Omega^2\left(x_1 \pm x_1^0\right)^2 \quad (12)$$

$$B = \sum_{i=2}^{M}\kappa_i x_i \quad (13)$$

$$V_b(x_2,..,x_M) = \frac{1}{2}\sum_{i=2}^{M}\widetilde{\omega_i}^2 x_i^2 \quad (14)$$

In these expressions, we have used the abbreviations $x_1^0 = \|\mathbf{c}\|$, $\Omega^2 = \mathbf{u}_1^T\mathbf{\Lambda}\mathbf{u}_1$ and $\kappa_j = \mathbf{u}_1^T\mathbf{\Lambda}\mathbf{u}_j$

This transformation thus represents the ET process as a electronic transfer coupled to a primary mode x_1, and coupled to a set of transformed bath modes $x_i, i = 2,\cdots M$.

A natural separation into system H_s and bath H_b can thus be written as:

$$H = H_s + S\cdot B + H_b \quad (15)$$

with

$$H_S = \begin{pmatrix} T_1 + W_L(x_1) & V_{LR} \\ V_{RL} & T_1 + W_R(x_1) \end{pmatrix} \quad (16)$$

$$S = \begin{pmatrix} x_1 + x_1^0 & 0 \\ 0 & x_1 - x_1^0 \end{pmatrix} \quad (17)$$

$$H_b = \begin{pmatrix} T_b + V_b(x_2,..,x_M) & 0 \\ 0 & T_b + V_b(x_2,..,x_M) \end{pmatrix} \quad (18)$$

This partitioning forms the basis of the dissipative treatment to be presented below.

5.2 Results of the reaction path model

We first remark that for each DMP_n molecule, the frequency Ω of the reaction path oscillator (Table 3) is very close to the frequency of the maxima in the $|d_i|$ distribution, as shown in Fig.3. As x_1^0 is the root mean square of the displacements of all the normal modes, it is a good quantity to assess how much the geometries are modified upon the charge transfer. It increases by a factor of almost 10 from DMP_0 to DMP_1 whereas it roughly remains constant from DMP_1 to DMP_2. This emphasizes the fact that the distorsion between the two DMP cycles initially implied by the bridge is more important than the one induced by adding another phenylene ring. This is in agreement with the findings based on the $|d_i|$ presented above.

To get a glimpse onto the mutual interplay between ET and nuclear deformation, we show the potential energy surface along the reaction path $W_{L/R}(x_1)$ as well as the corresponding adiabatic curves, obtained as

$$W_{\pm}^a(x_1) = \frac{1}{2}\left(W_L + W_R \pm \sqrt{(W_L - W_R)^2 + 4V_{LR}^2}\right) \quad (19)$$

The coordinate x_1, which describes the motion along the linear reaction path, interpolates between the two geometries, which are placed at the mimima of the two diabatic potentials $W_{L/R}(x_1)$, located at $x_1 = \pm x_1^0$ for $W_L(x_1)$ and $W_R(x_1)$ respectively.

The parabola $W_{L/R}(x_1)$ and $W_{\pm}^a(x_1)$ of the reaction path for each DMP_n are shown on figure 5. In each case, the diabatic representation $W_{L/R}(x_1)$ consists of two potential energy curves (parabolas in a harmonic model) crossing along the reaction path. However, one can easily link the shape of the adiabatic curves $W_{\pm}^a(x_1)$ to the Robin-Day classification scheme mentioned above. Indeed, as DMP_0 has a strong electronic coupling, the two parabolas disappear leading to an adiabatic potential with a single adiabatic minimum. This is in agreement with the class III character of this compound as the charge could be completely delocalized other the two sites. DMP_1 and DMP_2 have a weak electronic coupling leading to an adiabatic ground state potential energy curve with a double well. The charge could be partially localized according to the shape of the barrier. These are features of class II compounds. We also observe that the barrier is higher for DMP_2 than for DMP_1. The barriers are of 790 cm^{-1} and 1330 cm^{-1} for DMP_1 and DMP_2 respectively. This explains why experimentally, the charge in DMP_1 is more easily transferred than in the case of DMP_2.

As indicated earlier, a quantum dissipative treatment on the basis of perturbation theory using standard spin-boson model is not possible for the system considered in this work, due to the strong coupling of the electronic motion to the nuclear rearrangements. By including an overall geometical deformation into the system Hamiltonian, the coupling of this vibronic system to the remaining modes has been significantly reduced.

The distribution of the κ_i, the coupling constants of the reaction path to the remaining bath modes can be expressed in

Table 3 Reaction path frequency Ω and displacement x_1^0

	DMP_0	DMP_1	DMP_2
Ω (cm^{-1})	598	85	85
x_1^0 (a.u.)	63	617	650

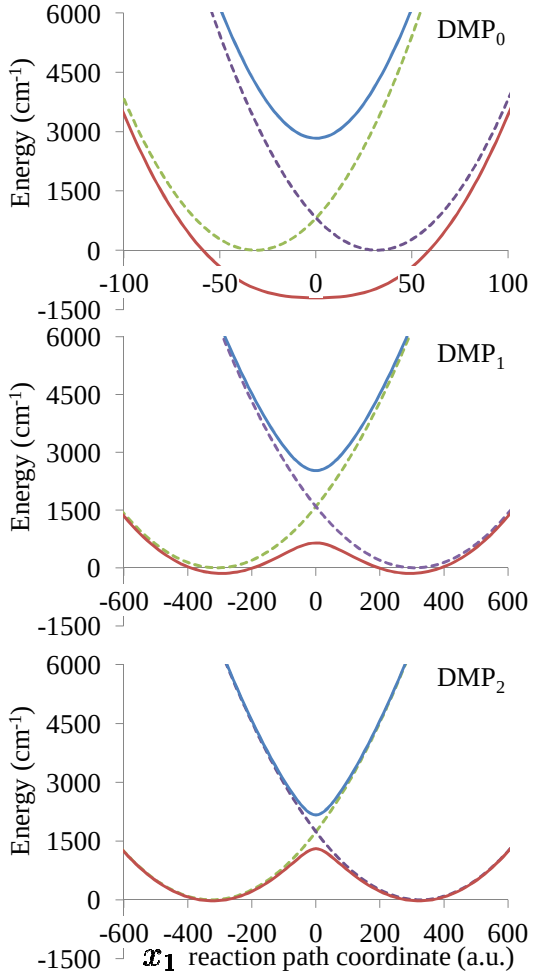

Fig. 5 Diabatic and adiabatic potential energy curves of the reaction path model for $DMP_{0,1,2}$. Plain red line : W_-^a Adiabatic ground state. Plain blue line : W_+^a Adiabatic excited state. Dashed green line : W_L Diabatic left state. Dashed violet line : W_R : Diabatic right state.

terms of a spectral density:

$$J(\omega) = \frac{\pi}{2}\sum_{i=2}^{M}\frac{\kappa_j^2}{\widetilde{\omega}_j}\delta(\omega-\widetilde{\omega}_j). \tag{20}$$

Following Ref.[8], to take solvent effects heuristically into account, and thus to construct a genuine dissipative theory, we express the spectral density as a smoothed function, i.e. approximate

$$\delta(\omega-\widetilde{\omega}_j) \approx \frac{1}{\pi}\frac{\Delta}{(\omega-\widetilde{\omega}_j)^2+\Delta^2} \tag{21}$$

with Δ obtained by the root mean square of the whole frequency distribution $\Delta = \sqrt{\sum_{j=2}^{M}(\widetilde{\omega}_{j+1}-\widetilde{\omega}_j)^2/(M-1)}$

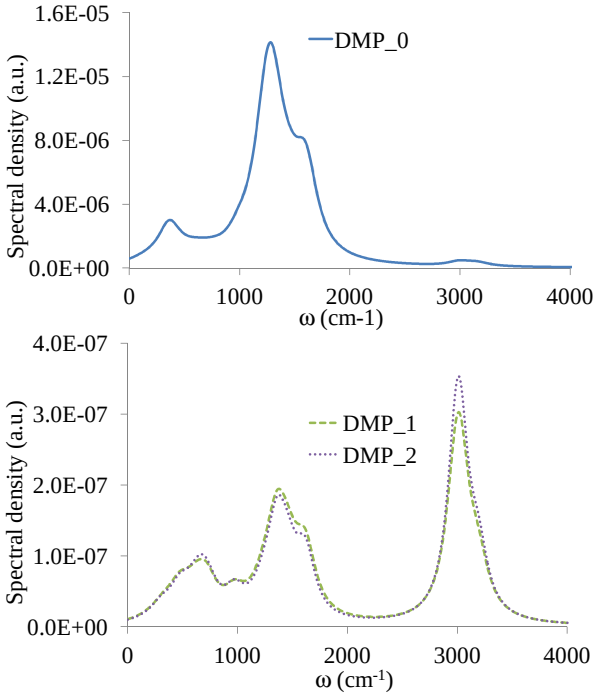

Fig. 6 Spectral density of the secondary modes in the reaction path model of $DMP_{0,1,2}$. Upper panel: DMP_0; lower panel: $DMP_{1,2}$. All these results have been obtained with the OPBE functional.

The resulting curves of $J(\omega)$ are depicted on Fig. 6. When comparing the results for DMP_0 with $DMP_{1,2}$ (lower panel), the most striking feature is the additional band around 3000 cm^{-1} which is due to the additional modes present stemming from the phenyl bridging fragments. This feature is consistent with the distribution of the normal mode displacements d_i, as explained in detail in Sec. 3, and clearly visible in Fig. 3.

6 Electron transfer quantum dynamics

In order to analyze the effects of nuclear motion onto the ET process, we choose a Redfield approach based on the above mentioned separation of a system containing the electronic degrees of freedom together with a one-dimensional motion along a chosen reaction path x_1, and a bath corresponding to the remaining nuclear displacements induced. These latter will be described by a thermal bath. To this end, we use the Nakajima-Zwanzig projector formalism to develop the quantum master equation.

6.1 Derivation of the master equation

Assuming the bath modes remain in thermal equilibrium $\rho_b^{(eq)} = \frac{1}{Z_b}e^{-\beta H_b}$ with $\beta = 1/k_BT$, these last ones induce a

dissipative dynamics of the system, described by the system density matrix :

$$\rho_S = \begin{pmatrix} \rho_{LL}(x_1,x_1') & \rho_{LR}(x_1,x_1') \\ \rho_{RL}(x_1,x_1') & \rho_{RR}(x_1,x_1') \end{pmatrix} . \quad (22)$$

Using the Nakajima-Zwanzig projector formalism[2,3], the time evolution of the density matrix elements is given by:

$$\dot{\rho}_S(t) = -i[H_S,\rho_S] + \int_0^t K(t-t')\rho_S(t')dt' \quad (23)$$

where initial system-bath correlation is neglected and the memory kernel can be expressed as:

$$K(t-t')\rho_S(t') = i\left[S,\{iC(t-t')U(t-t')S\rho_S(t')U^\dagger(t-t')\}+\{h.c.\}\right] \quad (24)$$

with $U(t-t') = e^{-iH_s(t-t')}$

At this level of approximation, the bath dynamics enters via the correlation function

$$C(t-t') = tr_b\left(Be^{+iH_b(t-t')}Be^{-iH_b(t-t')}\rho_b^{(eq)}\right) = \frac{1}{\pi}\int_{-\infty}^{\infty}\frac{J(\omega)e^{i\omega(t-t')}}{e^{\beta\omega}-1}d\omega \quad (25)$$

Eq. (23) can be further simplified. At the same level of perturbative order, we can replace $\rho_S(t') \approx U(t'-t)\rho_S(t)U^\dagger(t-t')$ to obtain a time-local memory kernel. The master equation then reads:

$$\dot{\rho}_S = -i[H_S,\rho_S] - \int_0^t d\tau\left\{C(\tau)\left[S,U(\tau)SU^\dagger(\tau)\rho_S(t)\right]\right\} - \{h.c.\} \quad (26)$$

where $\tau = t-t'$.

Since $C(\tau)$ is a function that decays to zero rapidly (in the order of 50 fs in our case), we can extend the upper integration limit to infinity (Markov approximation), an approximation which only affects the short-time behaviour, but not the relaxation on longer times. We thus arrive to the final equation:

$$\dot{\rho}_S = -i[H_S,\rho_S] - \left[S,\left\{D\rho_S(t)-\rho_S(t)D^\dagger\right\}\right] \quad (27)$$

with the dissipative operator given by

$$D = \int_0^\infty C(\tau)U(\tau)SU^\dagger(\tau)d\tau \quad (28)$$

In practice, equation (27) is solved in an eigenbasis of H_S, obtained by diagonalizing the 2-component Fourier grid Hamiltonian[106]. This diagonalisation yields vibronic states $|\chi_j\rangle$, with eigenenergies E_j. In this basis, H_S is diagonal, and the dissipative operator reads:

$$D_{ij} = S_{ij}\frac{J(\Delta E_{ij})}{e^{\beta\Delta E_{ij}}-1} \quad (29)$$

where ΔE_{ij} is the difference of energies of the two eigenvalues of the i^{th} and j^{th} eigenstates of the vibronic diagonalized basis set, and D_{ij} and S_{ij} are the matrix elements of D and S respectively. In obtaining this expression, the principal value parts of the integrals over the bath correlation functions have been neglected.

The time propagation is performed by a standard Runge-Kutta method, yielding ρ_S at all times, from which several observables of interest have been obtained. First, the population P_j of the system in the different vibronic eigenstate are simply given by:

$$P_j = \langle\chi_j|\rho_s|\chi_j\rangle . \quad (30)$$

From the full vibronic density matrix ρ_s, one can obtain an electronic density matrix by tracing out the vibrational degree of freedom x_1 to yield

$$\rho_S^{(el)} = \begin{pmatrix} \rho_{LL}^{(el)} & \rho_{LR}^{(el)} \\ \rho_{RL}^{(el)} & \rho_{RR}^{(el)} \end{pmatrix} \quad (31)$$

with

$$\rho_{\alpha\alpha'}^{(el)} = \int\rho_{\alpha\alpha'}(x_1,x_1)dx_1 \quad \alpha,\alpha' = L,R \quad (32)$$

where the electronic population in the left or right diabatic potential well describing the charge the corresponding part of the molecule given by $\rho_{LL}^{(el)}$ and $\rho_{RR}^{(el)}$ respectively, and the corresponding electronic coherence between the diabatic L/R states given by $\rho_{LR}^{(el)}$

Furthermore, we wish to analyze the nuclear dynamics along the reaction path, i.e. the position probability density

$$P(x_1) = \rho_{RR}(x_1,x_1)+\rho_{LL}(x_1,x_1) . \quad (33)$$

In analogy to the electronic decoherence, we also wish to analyze vibrational decoherence. An intuitive measure of vibrational coherence is the position expectation value

$$\langle x_1\rangle = \int x_1P(x_1)dx_1 \quad (34)$$

which shows a dynamical behaviour as long as the vibrational motion maintains coherences. This process of decoherence can be measured by analysing the loss of purity, which can be done by considering $tr\rho_S^2$. Indeed, this quantity equals one for a pure state, and is less than one for a statistical mixture. Hence, its decrease as a function of time is an indicator of decoherence.

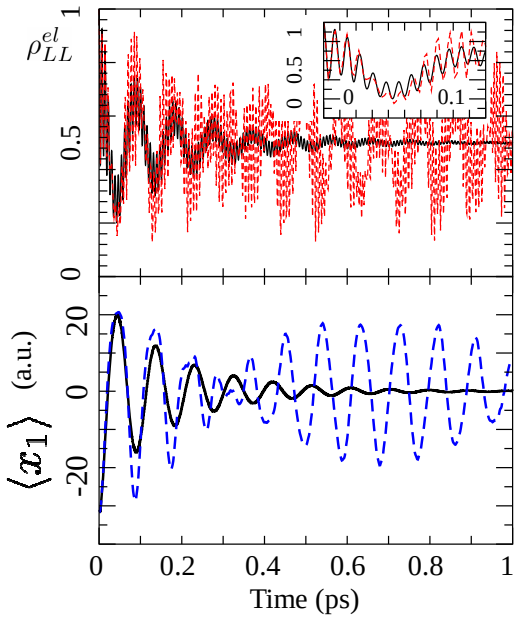

Fig. 7 Diabatic population and coherence estimated through the position expectation value $\langle x_1 \rangle$ of DMP_0 as a function of time ($T = 300K$). Top panel : Diabatic populations. Full lines: with dissipation, dashed line: without dissipation. Inset : Diabatic populations at shorter times. Bottom panel : full line $\langle x_1 \rangle$ with dissipation, dashed line $\langle x_1 \rangle$ without dissipation.

7 Results

To study the dynamics of electron transfer, and its interplay with the geometrical deformations, described by both the reaction path and the remaining bath modes, we consider the charge to be initially located on one side, i.e. the wavepacket is taken to be the vibrational ground state of V_L (see eq. (5)). Subsequently, by time propagation, we analyze the charge migration, and the induced dynamics describing the nuclear rearrangement for all three cases, DMP_0, DMP_1, and DMP_2.

7.1 DMP_0: Class III regime.

Fig. 7 shows the evolution of reduced density matrix element ρ_{LL}^{el}. The total electronic population in the diabatic state V_L thus represents the probability to find the charge localised at one end of the molecule. We find damped oscillations with two mean periods: a rapid one with 7.0 fs and a slower one with 88 fs which are both damped on the timescale of 500 fs. The fast oscillation corresponds to Rabi oscillations between the two electronic states. The origin of the slower one becomes evident when compared to the mean position of the reaction path $\langle x_1 \rangle$, as shown in the lower panel: one clearly sees that the slower oscillation corresponds to the oscillation of $\langle x_1 \rangle$, thus reflecting vibrational motion along the reaction

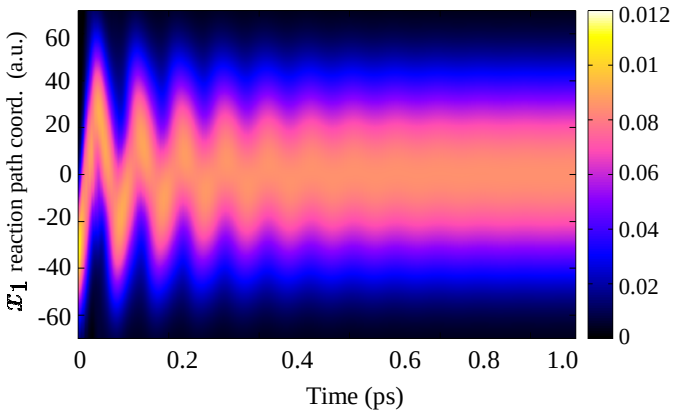

Fig. 8 Square root of position probability density $P(x_1)$ of DMP_0 as a function of time ($T = 300K$).

path, induced by the electron transfer. The oscillations of $\langle x_1 \rangle$ start from -30 a.u., which corresponds to the minimum of V_L (see Fig. 5). Both ρ_{LL}^{el} and $\langle x_1 \rangle$ show damped oscillations, with a time constant of about 500 fs. Specifically, the decrease of $\langle x_1 \rangle$ is a clear fingerprint of vibrational decoherence. To emphasize the role of the bath, these results have to be compared with the population and position expectation value without dissipation (dashed line on both respective panels of Fig. 7). Without secondary bath, the oscillations have the same two periods unless they do not reach an asymptotic behaviour and exhibit beating features expected for a wavepacket in a potential with a shape of an harmonic oscillator. Hence, the overall picture that arises from these results is a rapid charge oscillation, accompanied by periodic nuclear deformations, and this concerted vibronic dynamics shows a strong dissipation due to the coupling to the remaining bath modes. All these features are characteristics of a class III charge transfer system.

After about 1 ps, the system has reached thermal equilibrium, with ρ_{LL}^{el} levelling off at 0.5 and $\langle x_1 \rangle$ converging to zero. This indicates a complete charge delocalization over the whole molecule, and a relaxation to a symmetric geometry. The nuclear quantum dynamics can in more detail be seen in Fig. 8, where the probability distribution $P(x_1)$ (see eq. 33). is depicted for times up to 1 ps. At short times, we find a narrow wave packet, peaked around its expectation value, which undergoes damped oscillations and spreading. This vibrational motion is consistent with the potential energy surfaces depicted in Fig. 5 (upper panel). At equilibrium, the probability spreads over about 20 a.u.

To show that this state, both in terms of electronic population as well as in vibrational motion, is indeed the Boltzmann limit, we plot in Fig. 9 the population P_j of selected vibronic states $|\chi_j\rangle$, which are eigenstates of H_S. We clearly see how these populations tend to limits given by the Boltzmann distribution (shown at the right of Fig. 9). The Boltzmann distribu-

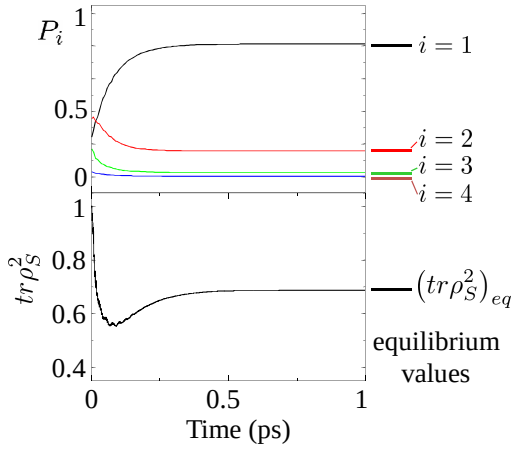

Fig. 9 Vibronic populations and purity of the reduced electronic density matrix of DMP_0 in function of time at $T = 300K$. The corresponding values in a Boltzmann ensemble are added on the right side.

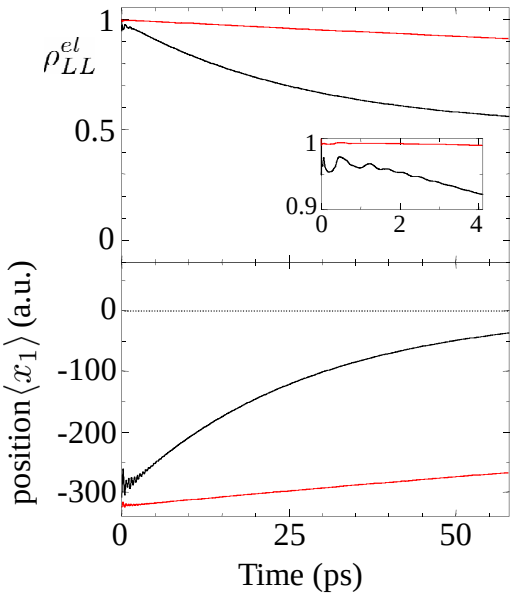

Fig. 10 Diabatic population (upper panel) and position expectation value $\langle x_1 \rangle$ (lower panel) of DMP_1 (black curve) and DMP_2 (red curve) in function of time at $T = 300K$.

tion comprises several states, i.e. is a statistical mixture, and as a consequence, the value of $tr\rho_S^2$ is less than one.

These features of a class III type ET, with charge and geometry relaxation with a rather rapid time constant of about 500 fs is due to the lack of a barrier along the reaction path, and is thus significantly different from DMP_1 and DMP_2, as will be shown in the following section.

7.2 $DMP_{1,2}$: Class II regime.

As shown in section 5.2, adding one (DMP_1) or two (DMP_2) bridge molecules leads to an adiabatic reaction path potential energy surface which exhibits a double minimum with a barrier. This leads to a significantly different charge transfer dynamics as compared to DMP_0, and the corresponding nuclear deformations. To analyze this dynamics, we perform the same calculations as in DMP_0: starting from a fully localized charge state, i.e. the vibrational ground state of V_L, we follow the vibronic dynamics by numerically solving eq. (27). The results are presented in Fig. 10 for DMP_1 (black curves) and DMP_2 (red curves). When comparing with the corresponding results for DMP_0 (Fig. 7), we find qualitative differences: in case of $DMP_{1,2}$, there are no oscillations, but slow relaxation towards charge equilibration, on a timescale of about 100 ps for DMP_1 and even longer for DMP_2. For very short times (see inset of Fig. 10), we find weak dynamical structures, before slow, continuous equilibration takes place. Again, charge dynamics is accompanied by nuclear rearrangements, as seen from the time evolution of $\langle x_1 \rangle$ (lower panel). Also in this graph, a weak dynamical behaviour is observed for very short times, before $\langle x_1 \rangle$ converges to zero on a timescale of about 100 ps for DMP_1. In case of DMP_2, both charge and nuclear dynamics are too slow to allow for reliable estimate of relaxation times within the calculated time window. In both cases, the fact that $\langle x_1 \rangle$ converges to zero does not mean however there is a maximum of the probability density around $x_1 = 0$. This can be seen on Fig. 11 showing the probability density $P(x_1)$ (as defined in eq. 33) as a function of time. Starting from a distribution initially well-localized around the minimum of $V_L(x_1)$, it reaches without any significant dynamics, a final bi-modal shape, reflecting the double minimum of the adiabatic potential energy surface $W_-^a(x_1)$. The lowest two eigenstates are degenerate (see table 5) and correspond to a maximum of localization probability in the right well for the ground state and on the left side for the second one. To analyze this dynamics in more detail, we show on Fig. 12 the populations P_j of the vibronic eigenstates of H_S for DMP_1. Starting from a non-equilibrium distribution, we see that within a short time of about 500 fs, the higher states have converged to their equilibrium values, and the long time coherent dynamics is entirely comprised within the subspace of the two lowest vibronic states.

To summarize, the barrier in the adiabatic potential energy surface along the reaction path x_1 dramatically modifies charge transfer and nuclear dynamics, and leads to strong charge localisation. Dynamics converges to equilibrated final charge distribution only very slowly, without any oscillations . These are characteristics of a class II ET system. While the higher states relax rapidly, the long time behaviour is entirely dominated by the states below the barrier, leading to the ob-

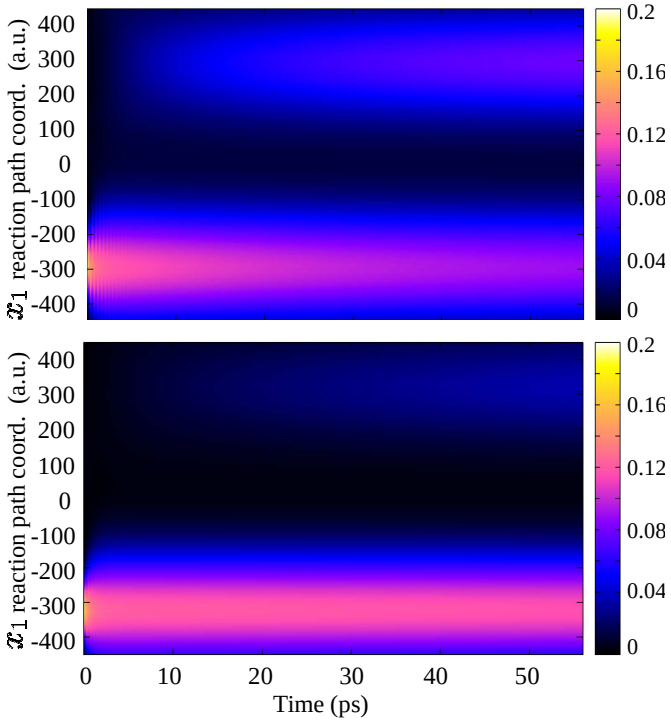

Fig. 11 Square root of position probability density $P(x_1)$ of $DMP_{1,2}$ over time ($T = 300K$). Top : DMP_1. Bottom : DMP_2.

served very slow charge equilibration.

7.3 Temperature effects.

Temperature effects are very different between class III and class II. This is illustrated through the population P_i in the initial and equilibrium vibronic states for DMP_0 in Tab. 4 and DMP_1 in Tab. 5 and both through the evolution of the average position $\langle x_1 \rangle$ shown in Fig. 13.

Table 4 Energy E_{vib} and expected values of the population P_{vib} of vibronic states of DMP_0 for initial state $P_{vib,0}$ and for Boltzmann equilibrium $P_{vib,eq}$ at different temperatures.

	1	2	3	4
E_{vib} (cm^{-1})	-1034	-692.0	-301.2	112.3
$P_{vib,0}$	0.242	0.355	0.170	$3.07\ 10^{-2}$
$P_{vib,eq}$ (300 K)	0.814	0.158	0.024	0.003
$P_{vib,eq}$ (50 K)	0.999	$5.29\ 10^{-5}$	$6.91\ 10^{-10}$	$4.70\ 10^{-15}$

The bath temperature has a very small effect on the relaxation dynamics for class III system. Indeed, initial nuclear wave function (ground state of $W_L(x_1)$) is mainly a superposition of the first four vibronic eigenstates. As shown in Tab. 4, the weights of the excited vibronic states (about forty) are very small. Relaxation then requires only few transitions and

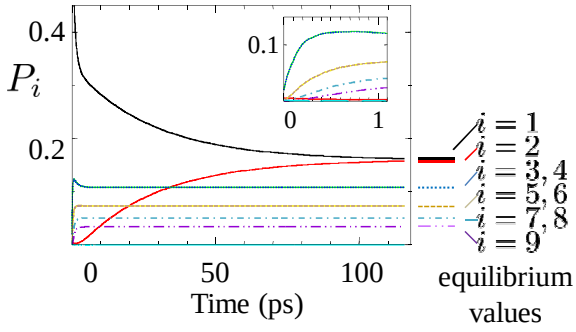

Fig. 12 Vibronic populations P_i of DMP_1 over time ($T = 300K$). The Boltzmann values are given at the right side. In the inset, the same figure between 0 and 1 ps.

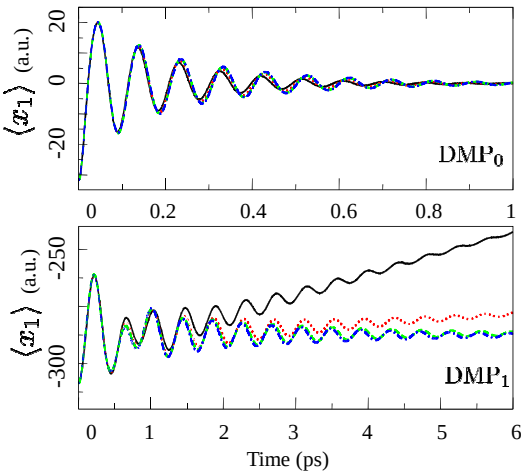

Fig. 13 Position expectation value of $DMP_{0,1}$ at different temperatures. Top panel : DMP_0. Bottom panel : DMP_1. Plain black line : 300 K. Red dotted line : 200 K. Dashed green line : 120 K. Dashed and dotted blue line : 50 K.

decoherence seen in the damped evolution of the mean position operates on similar timescale for all temperatures.

On the contrary, as shown in Fig.13, relaxation with class II (DMP_1) strongly depends on temperature. In this case, the ground adiabatic potential energy curve presents a double well shape and vibronic states below the barrier appear in well-known tunneling doublets (see table 5). For DMP_1, due to the barrier width, the ground-level vibronic eigenfunctions remain localized in only one potential well with a small secondary maximum on the other side. Higher-lying states are more delocalized across both potential wells. Under these circumstances, the initial vibrational wave function has components only on the vibronic state localized in the left side, as clearly seen from Tab. 5. The interaction with the thermal bath leads to redistribution of the population across the

Table 5 Energy E_{vib} and expected values of the population P_{vib} of vibronic states of DMP_1 for initial state $P_{vib,0}$ and for Boltzmann equilibrium $P_{vib,eq}$ at different temperatures.

	1	2	3	4
E_{vib} (cm^{-1})	-97.25	-97.25	-15.9	-15.9
$P_{vib,0}$	0.935	$4.82\ 10^{-3}$	$1.93\ 10^{-2}$	$1.94\ 10^{-2}$
$P_{vib,eq}$ (300 K)	0.159	0.159	0.108	0.108
$P_{vib,eq}$ (50 K)	0.452	0.452	0.043	0.043

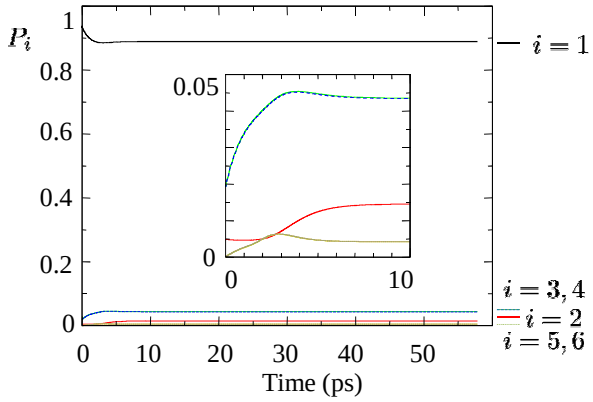

Fig. 14 Vibronic populations P_i of DMP_1 as a function of time at temperature of $T = 50K$. In the inset, the same figure between 0 and 10 ps.

vibronic states. For instance, the transfers to states 3 and 4 from state 1 are very efficient, since these transitions exhibit strong matrix elements and $J(\Delta E_{ij})$ is non-zero, and thus leads to a quick thermalization of these two states. This behaviour is similar for higher energy states as shown in Fig. 12. At 300 K, the last vibronic state populated with more than 0.1 % of the total population is the twenty-eighth (920 cm^{-1}). This vibronic state is over the barrier and almost delocalized over the left and right electronic states. A direct population transfer for $1 \rightarrow 2$ is strongly suppressed since 1 and 2 are quasi-degenerate with a negligible coupling element. The transfer between the two first states thus proceeds via vibrational excited states. These higher energy states over the barrier open an indirect gate for a stationary population transfer from the first to the second although these two are both localized vibronic states. It thus strongly depends on the vibronic population P_i distribution with temperature. This can clearly be seen in Fig. 14, which is the same as Fig. 12, but for a temperature of 50 K. At this temperature, the states 3 and 4 are only weakly populated and the last level populated with more than 0.1% of the total population is only the sixth (145 cm^{-1}) which is below the barrier. This leads to a trapping of the vibronic populations what is also clearly visible in the position expectation value $\langle x_1 \rangle$.

Conclusions

In this work, we have analyzed charge transfer dynamics of mixed-valence compounds using time dependent dissipative quantum simulations. One aim was to present the methodology: first, the contrained DFT framework allowed us to determine the nuclear reorganizations that accompany the charge transfer within a diabatic picture. Geometrical deformations induced by electron transfer were found to be in good agreement with experimental results. However, electronic couplings were parameterized. On the basis of these electronic structure calculations, a quantum dynamical approach was developed, to study the combined charge transfer / vibrational dynamics in its full dimensionality, and heuristically including solvent effects. The dissipative quantum dynamics is based on the Redfield approach. However, a thourough analysis revealed that the coupling between charge transfer and nuclear deformations was too strong to be treated perturbatively within the standard spin-boson model. We thus developed a reaction path model, in which a linear interpolation of two limiting geometries has been used as reaction path to be included into the system Hamiltonian. Through this methodology, the coupling to the remaining modes has been reduced allowing for a subsequent perturbative treatment of the remaining bath modes. The dynamical approach thus consisted in a dissipative combined electronic/vibrational propagation, within a Redfield approach, where the dissipative operators are entirely determined from first principles without any adjustable parameters.

Specifically, for the system under study, we have analyzed the influence of a different number of bridge molecules onto the charge transfer dynamics. In each regime, relaxation towards equilibrium has been discussed in terms of the occupation of the stationary vibronic eigenstates. It is the superposition of these eigenstates which undergoes decoherence and by projection we get view on the partial diabatic or adiabatic electronic or vibrational decoherence.

For DMP_0, without bridge, charge transfer proceeds along the reaction path on a barrierless adiabatic potential energy surface. It has all the features of a class III system. The detailed calculations including the dissipation yielded a timescale of both geometry and charge relaxation of about 500 fs towards a fully symmetric geometry with a delocalized charge distribution.

For $DMP_{1,2}$, bridge molecules lead to a barrier along the reaction path, which drastically changes the charge transfer dynamics (class II system): the charge does not oscillate, but only very slowly relaxes to its final distribution. While the short time behaviour might show some rapid dynamics, which stem from the preparation of the initial state, the long time behaviour is entirely dominated by the lowest vibronic states within the double well potential. For high barriers, where the

tunnel splitting is very small, the charge and geometry relaxation is extremely slow, even in the presence of a bath.

We think the proposed methodology, applied to model systems in this work, is well suited to analyze the subtle interplay between charge transfer and nuclear deformations, a prototype situation for many important processes in chemical and biological systems where both electronic and vibrational decoherences proceed in a similar time scale. In these more general cases, the following treatment can be applied.

First, one of the crucial issue is how to choose a correct partitioning between system and bath for a given problem. The partitioning of the initial spin-boson model usually invalidates any dynamical perturbative treatment so that at least one collective mode has to be included into the system in order to reduce the coupling. The main manipulation is then a canonical transformation of the spin-boson vibrational bath. A similar procedure could be used when charge transfer occurs in photovoltaic materials or in solid matrices or in crystalline bulk structure if a sufficiently large sample of the environment can be treated by the DFT approach. In solid state, the initial phonon spectral density could also be described by smooth ohmic or superohmic densities calibrated from experimental measurements. In that case, our procedure should begin by a discretization of this spin-boson spectral density. For ET in larger systems encountered in life science such as ET in proteins or nucleic acid, alternative strategies will be required. First, because an exhaustive treatment by cDFT is not conceivable for systems composed of thousands of atoms. Hybrid QM/MM approach by which only the most important molecular fragments (e.g. the Donor-Bridge-Acceptor system) are treated by DFT while the remaining atoms are treated by molecular mechanics force fields is well established to handle large systems. Actually, the main difficulty would lie in the calculation of normal modes for very large systems, let alone the inclusion of non-harmonic effects that may be important for biological electron transfer. To circumvent these difficulties, an appealing procedure would be to calibrate the spectral densities from the time correlation function of the fluctuation of the electronic energy gap[39,107–109]. The latter can be straightforwardly obtained from molecular dynamics simulations. As explained for instance in ref.[110], the classical correlation function can be corrected to account for the oscillator Bose distribution. The continuous spin-boson spectral density should then be discretized and transformed to apply the collective mode model. A prolongation of the present work to model ET in large and complex molecular systems would thus to resort to hybrid cDFT/MM MD simulations from which spin-boson spectral densities could be calibrated. We are working in our laboratories on this strategies and will report our results in due course.

Acknowledgments

We are grateful to Daniel Mejía-Rodrígues and Andreas M. Köster for providing us before public release with fortran subtroutines to compute Fock exchange contributions in deMon2k.

This work has been performed within the French research network GDR 3575 THEMS.

Appendix : Reaction path formalism

In the two-level system case, from a spin-boson Hamiltonian written in mass-weighted coordinates, one can write :

$$H = \begin{pmatrix} T + V_L(\mathbf{q}) & V_{LR} \\ V_{LR} & T + V_R(\mathbf{q}) \end{pmatrix}$$

with $T = \frac{1}{2}\sum_{i=1}^{M} -\frac{\partial^2}{\partial q_i^2}$ and $V_{R/L}(\mathbf{q}) = \frac{1}{2}\sum_{i=1}^{M} \omega_i^2 \left(q_i \pm d_i/2\right)^2$ where we have defined the vector $\mathbf{q} = (q_1, \cdots, q_M)$.

We proceed by defining a linear reaction path $\mathbf{u}_1 = \mathbf{c}/\|\mathbf{c}\|$ where $\mathbf{c} = \sum_i (d_i/2)\,\mathbf{e_i}$ in order to manage a coordinate change $\{q_i\} \rightarrow \{x_1, x_i\}$ through a vectorial transformation from $\{\mathbf{e}_i\} \rightarrow \{\mathbf{u}_i\}$. $\mathbf{u}_1$ is a normalized reaction path vector. The secondary modes $\left\{\mathbf{u}_i / i \in [\![2, M]\!]\right\}$ are constructed normalized and orthogonal to this one (as well as orthogonal in their own space). The potential energy operator can be written as : $V_{R/L} = \frac{1}{2}(\mathbf{q} \pm \mathbf{c})^T \mathbf{\Lambda} (\mathbf{q} \pm \mathbf{c})$ where $\mathbf{q} = \sum_{i=1}^{M} x_i \mathbf{u}_i$ in the new basis set. We set $\|\mathbf{c}\| = x_1^0$ and $\Lambda_{ij} = \delta_{ij}\omega_i^2$.

$$V_{R/L} = \frac{1}{2}\left(\left(x_1 \pm x_1^0\right)\mathbf{u}_1 + \sum_{i=2}^{M} x_i \mathbf{u}_i\right)^T \mathbf{\Lambda} \left(\left(x_1 \pm x_1^0\right)\mathbf{u}_1 + \sum_{i=2}^{M} x_i \mathbf{u}_i\right)$$
$$= \frac{1}{2}\left[\begin{array}{l} {\mathbf{u}_1}^T \mathbf{\Lambda} \mathbf{u}_1 \left(x_1 \pm x_1^0\right)^2 + \sum_{i=2}^{M}\sum_{j=2}^{M} x_i x_j {\mathbf{u}_i}^T \mathbf{\Lambda} \mathbf{u}_j \\ + \sum_{i=2}^{M} x_i \left(x_1 \pm x_1^0\right)\left({\mathbf{u}_1}^T \mathbf{\Lambda} \mathbf{u}_i + {\mathbf{u}_i}^T \mathbf{\Lambda} \mathbf{u}_1\right) \end{array}\right]$$

We define a projector on the reaction path $\mathbf{P} = \mathbf{u}_1 {\mathbf{u}_1}^T$ and orthogonal to this one $\mathbf{Q} = \mathbf{I} - \mathbf{P}$ in order to express the $\mathbf{P\Lambda P}$, $\mathbf{Q\Lambda Q}$ matrices. After diagonalization, $\mathbf{P\Lambda P}$ leads to one non-zero eigenvalue Ω^2 of the reaction path (eigenvector) $\mathbf{u}_1$ and $\mathbf{Q\Lambda Q}$ to a $M-1$ non-zero eigenvalues ${\widetilde{\omega}_i}^2$ of the secondary bath modes (eigenvectors) $\left\{\mathbf{u}_i / i \in [\![2, M]\!]\right\}$. The couplings κ_i are then calculated through $\mathbf{P\Lambda Q} + \mathbf{Q\Lambda P}$ expressed in the basis of the $\{\mathbf{u}_i\}$.

References

1 A. Nitzan, *Chemical Dynamics in Condensed Phases : Relaxation, Transfer and Reactions in Condensed Molecular Systems*, Oxford University Press, 2006.

2 V. May and O. Kühn, *Charge and Energy Transfer Dynamics in Molecular Systems*, John Wiley & Sons, 2008.
3 U. Weiss, *Quantum Dissipative Systems*, World Scientific, 2012.
4 M. Bixon and J. Jortner, *Advances in Chemical Physics*, John Wiley & Sons, Inc., 1999, pp. 35–202.
5 *Energy Transfer Dynamics in Biomaterial Systems*, ed. I. Burghardt, V. May, D. A. Micha and E. R. Bittner, Springer Berlin Heidelberg, Berlin, Heidelberg, 2009, vol. 93.
6 J. Li, H. Wang, P. Persson and M. Thoss, *J. Chem. Phys.*, 2012, **137**, 22A529.
7 H. Tamura, I. Burghardt and M. Tsukada, *J. Phys. Chem. C*, 2011, **115**, 10205–10210.
8 H. Tamura, R. Martinazzo, M. Ruckenbauer and I. Burghardt, *J. Chem. Phys.*, 2012, **137**, 22A540.
9 A. Chenel, E. Mangaud, I. Burghardt, C. Meier and M. Desouter-Lecomte, *J. Chem. Phys.*, 2014, **140**, 044104.
10 K. H. Hughes, B. Cahier, R. Martinazzo, H. Tamura and I. Burghardt, *Chem. Phys.*, 2014, **442**, 111–118.
11 I. Franco and P. Brumer, *J. Chem. Phys.*, 2012, **136**, 144501.
12 E. Collini, C. Y. Wong, K. E. Wilk, P. M. G. Curmi, P. Brumer and G. D. Scholes, *Nature*, 2010, **463**, 644–647.
13 A. Ishizaki, T. R. Calhoun, G. S. Schlau-Cohen and G. R. Fleming, *Phys. Chem. Chem. Phys.*, 2010, **12**, 7319–7337.
14 G. S. Engel, T. R. Calhoun, E. L. Read, T.-K. Ahn, T. Mančal, Y.-C. Cheng, R. E. Blankenship and G. R. Fleming, *Nature*, 2007, **446**, 782–786.
15 G. D. Scholes and C. Smyth, *J. Chem. Phys.*, 2014, **140**, 110901.
16 E. Collini and G. D. Scholes, *Science*, 2009, **323**, 369–373.
17 A. Garg, J. N. Onuchic and V. Ambegaokar, *J. Chem. Phys.*, 1985, **83**, 4491–4503.
18 A. J. Leggett, S. Chakravarty, A. T. Dorsey, M. P. A. Fisher, A. Garg and W. Zwerger, *Rev. Mod. Phys.*, 1987, **59**, 1–85.
19 J. E. Subotnik, S. Yeganeh, R. J. Cave and M. A. Ratner, *J. Chem. Phys.*, 2008, **129**, 244101.
20 J. E. Subotnik, R. J. Cave, R. P. Steele and N. Shenvi, *J. Chem. Phys.*, 2009, **130**, 234102.
21 W.-L. Chan, T. C. Berkelbach, M. R. Provorse, N. R. Monahan, J. R. Tritsch, M. S. Hybertsen, D. R. Reichman, J. Gao and X.-Y. Zhu, *Acc. Chem. Res.*, 2013, **46**, 1321–1329.
22 J. Li, M. Nilsing, I. Kondov, H. Wang, P. Persson, S. Lunell and M. Thoss, *J. Phys. Chem. C*, 2008, **112**, 12326–12333.
23 C.-P. Hsu, P. J. Walla, M. Head-Gordon and G. R. Fleming, *J. Phys. Chem. B*, 2001, **105**, 11016–11025.
24 H.-C. Chen, Z.-Q. You and C.-P. Hsu, *J. Chem. Phys.*, 2008, **129**, 084708.
25 C.-P. Hsu, Z.-Q. You and H.-C. Chen, *J. Phys. Chem. C*, 2008, **112**, 1204–1212.
26 C.-P. Hsu, *Acc. Chem. Res.*, 2009, **42**, 509–518.
27 D. Ambrosek, A. Köhn, J. Schulze and O. Kühn, *J. Phys. Chem. A*, 2012, **116**, 11451–11458.
28 L. Song and J. Gao, *J. Phys. Chem. A*, 2008, **112**, 12925–12935.
29 T. Wesolowski, R. P. Muller and A. Warshel, *J. Phys. Chem.*, 1996, **100**, 15444–15449.
30 A. Warshel, *J. Phys. Chem.*, 1982, **86**, 2218–2224.
31 A. Warshel and J.-K. Hwang, *J. Chem. Phys.*, 1986, **84**, 4938–4957.
32 P. H. Dederichs, S. Blügel, R. Zeller and H. Akai, *Phys. Rev. Lett.*, 1984, **53**, 2512–2515.
33 Q. Wu and T. Van Voorhis, *Phys. Rev. A*, 2005, **72**, 024502.
34 T. Van Voorhis, T. Kowalczyk, B. Kaduk, L.-P. Wang, C.-L. Cheng and Q. Wu, *Annu. Rev. Phys. Chem.*, 2010, **61**, 149–170.
35 N. Makri and D. E. Makarov, *J. Chem. Phys.*, 1995, **102**, 4600–4610.
36 C. H. Mak, *Phys. Rev. Lett.*, 1992, **68**, 899–902.
37 Y. Tanimura and R. Kubo, *J. Phys. Soc. Jpn.*, 1989, **58**, 101–114.
38 Y. Tanimura, *J. Phys. Soc. Jpn.*, 2006, **75**, 082001.
39 D. Xu and K. Schulten, *Chemical Physics*, 1994, **182**, 91–117.
40 M. Tanaka and Y. Tanimura, *J. Chem. Phys.*, 2010, **132**, 214502.
41 H. D. Meyer, U. Manthe and L. S. Cederbaum, *Chemical Physics Letters*, 1990, **165**, 73–78.
42 U. Manthe, H.-D. Meyer and L. S. Cederbaum, *J. Chem. Phys.*, 1992, **97**, 3199–3213.
43 M. H. Beck, A. Jäckle, G. A. Worth and H. D. Meyer, *Physics Reports*, 2000, **324**, 1–105.
44 H.-D. Meyer, F. Gatti and G. A. Worth, *Multidimensional Quantum Dynamics*, John Wiley & Sons, 2009.
45 M. Thoss, I. Kondov and H. Wang, *Phys. Rev. B*, 2007, **76**, 153313.
46 U. Manthe, *J. Chem. Phys.*, 2008, **128**, 164116.
47 U. Manthe, *J. Chem. Phys.*, 2009, **130**, 054109.
48 O. Vendrell and H.-D. Meyer, *J. Chem. Phys.*, 2011, **134**, 044135.
49 E. Pollak, *J. Chem. Phys.*, 1986, **85**, 865–867.
50 J. Cao and G. A. Voth, *J. Chem. Phys.*, 1997, **106**, 1769–1779.
51 A. Pereverzev, E. R. Bittner and I. Burghardt, *J. Chem. Phys.*, 2009, **131**, 034104.
52 K. H. Hughes, C. D. Christ and I. Burghardt, *J. Chem. Phys.*, 2009, **131**, 124108.
53 R. A. Marcus, *Rev. Mod. Phys.*, 1993, **65**, 599–610.
54 A. M. Levine, M. Shapiro and E. Pollak, *J. Chem. Phys.*, 1988, **88**, 1959–1966.
55 V. Chernyak and S. Mukamel, *J. Chem. Phys.*, 1996, **105**, 4565–4583.
56 J. Cao, *J. Chem. Phys.*, 1997, **107**, 3204–3209.
57 R. Martinazzo, B. Vacchini, K. H. Hughes and I. Burghardt, *J. Chem. Phys.*, 2011, **134**, 011101.
58 I. Burghardt, R. Martinazzo and K. H. Hughes, *J. Chem. Phys.*, 2012, **137**, 144107.
59 H.-D. Meyer and W. H. Miller, *J. Chem. Phys.*, 1979, **70**, 3214–3223.
60 P. Huo, T. F. M. Iii and D. F. Coker, *J. Chem. Phys.*, 2013, **139**, 151103.
61 S. J. Cotton, K. Igumenshchev and W. H. Miller, *J. Chem. Phys.*, 2014, **141**, 084104.
62 J. M. Moix and J. Cao, *J. Chem. Phys.*, 2013, **139**, 134106.
63 X. Zhong and Y. Zhao, *J. Chem. Phys.*, 2013, **138**, 014111.
64 M. Thoss, H. Wang and W. H. Miller, *J. Chem. Phys.*, 2001, **115**, 2991–3005.
65 A. Redfield, *IBM J. Res. Dev.*, 1957, **1**, 19–31.
66 A. G. Redfield, *Advances in Magnetic and Optical Resonance*, Academic Press, 1965, vol. 1, pp. 1–32.
67 W. T. Pollard, A. K. Felts and R. A. Friesner, *Advances in Chemical Physics*, John Wiley & Sons, Inc., 1996, pp. 77–134.
68 R. Schneider, W. Domcke and H. Köppel, *J. Chem. Phys.*, 1990, **92**, 1045–1061.
69 D. Egorova, M. Thoss, W. Domcke and H. Wang, *J. Chem. Phys.*, 2003, **119**, 2761–2773.
70 D. Egorova, A. Kühl and W. Domcke, *Chemical Physics*, 2001, **268**, 105–120.
71 A. Palii, C. Bosch-Serrano, J. M. Clemente-Juan, E. Coronado and B. Tsukerblat, *J. Chem. Phys.*, 2013, **139**, 044304.
72 C. Meier and D. J. Tannor, *J. Chem. Phys.*, 1999, **111**, 3365–3376.
73 A. Pomyalov, C. Meier and D. J. Tannor, *Chemical Physics*, 2010, **370**, 98–108.
74 U. Kleinekathöfer, *J. Chem. Phys.*, 2004, **121**, 2505–2514.
75 M. Schröder, U. Kleinekathöfer and M. Schreiber, *J. Chem. Phys.*, 2006, **124**, 084903.
76 J. Hankache and O. S. Wenger, *Chem. Rev.*, 2011, **111**, 5138–5178.
77 S. V. Rosokha, D.-L. Sun and J. K. Kochi, *J. Phys. Chem. A*, 2002, **106**, 2283–2292.

78 S. V. Lindeman, S. V. Rosokha, D. Sun and J. K. Kochi, *J. Am. Chem. Soc.*, 2002, **124**, 843–855.

79 M. B. Robin and P. Day, *Advances in Inorganic Chemistry and Radiochemistry*, Academic Press, 1968, vol. 10, pp. 247–422.

80 A. de la Lande and D. R. Salahub, *J. Mol. Struct. THEOCHEM*, 2010, **943**, 115–120.

81 J. Řezáč, B. Lévy, I. Demachy and A. de la Lande, *J. Chem. Theory Comput.*, 2012, **8**, 418–427.

82 A. M. Köster, P. Calaminici, M. E. Casida, R. Flores-Moreno, G. Geudtner, A. Goursot, T. Heine, A. Ipatov, F. Janetzko, J. M. del Campo, S. Patchkovskii, J. Ulises Reveles, D. R. Salahub, A. Vela and deMon developers, *deMon2k*, 2006.

83 A. M. Köster, J. U. Reveles and J. M. d. Campo, *J. Chem. Phys.*, 2004, **121**, 3417–3424.

84 N. Godbout, D. R. Salahub, J. Andzelm and E. Wimmer, *Can. J. Chem.*, 1992, **70**, 560–571.

85 P. Calaminici, F. Janetzko, A. M. Köster, R. Mejia-Olvera and B. Zuniga-Gutierrez, *J. Chem. Phys.*, 2007, **126**, 044108.

86 M. Krack and A. M. Köster, *J. Chem. Phys.*, 1998, **108**, 3226–3234.

87 W.-M. Hoe, A. J. Cohen and N. C. Handy, *Chem. Phys. Lett.*, 2001, **341**, 319–328.

88 J. P. Perdew, K. Burke and M. Ernzerhof, *Phys. Rev. Lett.*, 1996, **77**, 3865–3868.

89 C. Lee, W. Yang and R. G. Parr, *Phys. Rev. B*, 1988, **37**, 785–789.

90 Y. Zhang and W. Yang, *Phys. Rev. Lett.*, 1998, **80**, 890–890.

91 A. D. Becke, *J. Chem. Phys.*, 1993, **98**, 5648–5652.

92 C. Adamo and V. Barone, *J. Chem. Phys.*, 1999, **110**, 6158–6170.

93 D. Mejia-Rodriguez and A. M. Köster, *J. Chem. Phys.*, 2014, **141**, 124114.

94 Q. Wu and T. V. Voorhis, *J. Chem. Phys.*, 2006, **125**, 164105.

95 F. L. Hirshfeld, *Theor. Chim. Acta*, 1977, **44**, 129–138.

96 Q. Wu and T. Van Voorhis, *J. Phys. Chem. A*, 2006, **110**, 9212–9218.

97 M. J. Frisch, G. W. Trucks, H. B. Schlegel, G. E. Scuseria, M. A. Robb, J. R. Cheeseman, G. Scalmani, V. Barone, B. Mennucci, G. A. Petersson, H. Nakatsuji, M. Caricato, X. Li, H. P. Hratchian, A. F. Izmaylov, J. Bloino, G. Zheng, J. L. Sonnenberg, M. Hada, M. Ehara, K. Toyota, R. Fukuda, J. Hasegawa, M. Ishida, T. Nakajima, Y. Honda, O. Kitao, H. Nakai, T. Vreven, J. A. Montgomery, Jr., J. E. Peralta, F. Ogliaro, M. Bearpark, J. J. Heyd, E. Brothers, K. N. Kudin, V. N. Staroverov, R. Kobayashi, J. Normand, K. Raghavachari, A. Rendell, J. C. Burant, S. S. Iyengar, J. Tomasi, M. Cossi, N. Rega, J. M. Millam, M. Klene, J. E. Knox, J. B. Cross, V. Bakken, C. Adamo, J. Jaramillo, R. Gomperts, R. E. Stratmann, O. Yazyev, A. J. Austin, R. Cammi, C. Pomelli, J. W. Ochterski, R. L. Martin, K. Morokuma, V. G. Zakrzewski, G. A. Voth, P. Salvador, J. J. Dannenberg, S. Dapprich, A. D. Daniels, Ö. Farkas, J. B. Foresman, J. V. Ortiz, J. Cioslowski and D. J. Fox, *Gaussian~09 Revision D.01*, Gaussian Inc. Wallingford CT 2009.

98 J.-D. Chai and M. Head-Gordon, *Phys. Chem. Chem. Phys.*, 2008, **10**, 6615.

99 Y. Zhao and D. G. Truhlar, *J. Phys. Chem. A*, 2006, **110**, 13126–13130.

100 V. Riffet, D. Jacquemin, E. Cauët and G. Frison, *J. Chem. Theory Comput.*, 2014, **10**, 3308–3318.

101 H. M. McConnell, *J. Chem. Phys.*, 1961, **35**, 508–515.

102 M. D. Newton, *Chem. Rev.*, 1991, **91**, 767–792.

103 R. Borrelli and A. Peluso, *J. Chem. Phys.*, 2003, **119**, 8437–8448.

104 K. H. Hughes, C. D. Christ and I. Burghardt, *J. Chem. Phys.*, 2009, **131**, 024109.

105 E. Gindensperger, I. Burghardt and L. S. Cederbaum, *J. Chem. Phys.*, 2006, **124**, 144103.

106 C. C. Marston and G. G. Balint-Kurti, *J. Chem. Phys.*, 1989, **91**, 3571–3576.

107 C. Olbrich, J. Strümpfer, K. Schulten and U. Kleinekathöfer, *J. Phys. Chem. Lett.*, 2011, **2**, 1771–1776.

108 A. Damjanović, I. Kosztin, U. Kleinekathöfer and K. Schulten, *Phys. Rev. E*, 2002, **65**, 031919.

109 C. Olbrich and U. Kleinekathöfer, *J. Phys. Chem. B*, 2010, **114**, 12427–12437.

110 S. Valleau, A. Eisfeld and A. Aspuru-Guzik, *J. Chem. Phys.*, 2012, **137**, 224103.